

Key Points:

- The sharp increase of the heat exchange at air-water interface at winds exceeding 33–35 m/s for stable and unstable air flow stratification was observed
- The universal dependency of the exchange coefficients and the temperature roughness on the peak wave number of surface wave spectra was found
- The correlation of the sharp increase in the air-water heat exchange with increased whitecapping was observed

Correspondence to:

Y. Troitskaya,
yuliya@hydro.appl.sci-nnov.ru

Citation:

Troitskaya, Y., Sergeev, D., Vdovin, M., Kandaurov, A., Ermakova, O., & Takagaki, N. (2020). A laboratory study of the effect of surface waves on heat and momentum transfer at high wind speeds. *Journal of Geophysical Research: Oceans*, 125, e2020JC016276. <https://doi.org/10.1029/2020JC016276>

Received 26 MAR 2020

Accepted 2 JUN 2020

Accepted article online 5 JUN 2020

A Laboratory Study of the Effect of Surface Waves on Heat and Momentum Transfer at High Wind Speeds

Yuliya Troitskaya^{1,2} , Daniil Sergeev¹ , Maksim Vdovin¹ , Alexander Kandaurov¹ , Olga Ermakova¹ , and Naohisa Takagaki³ 

¹Institute of Applied Physics, Nizhny Novgorod, Russia, ²A.M. Obukhov Institute of Atmospheric Physics, Moscow, Russia, ³Department of Mechanical Engineering, University of Hyogo, Himeji, Japan

Abstract This paper describes laboratory experiments (using a high-speed wind-wave flume) of the effects of water waves on heat and momentum exchange in the near-water atmospheric boundary layer at high wind speeds. Different from previous experiments of this type, the parameters of waves were controlled by a net stretched along the entire channel to effectively decrease the fetch. This helped to achieve dependency of the transfer coefficients on two independent parameters, namely, the wind speed and fetch (expressed via variations of the wavefield). Another key to the experiment was using a stable temperature stratification of the air flow, with the temperature of the air entering the flume 15–25° higher than the water. The experiments showed a sharp increase in the heat exchange coefficient at winds exceeding 33–35 m/s, similar to that observed earlier in the high-speed wind-wave flume of Kyoto University with conditions of unstable temperature stratification of the air flow. The joint analysis of the data obtained in the high-speed wind-wave flumes of IAP RAS and Kyoto University yields the universal dependency of the exchange coefficients and the temperature roughness on the peak wave number of surface wave spectra. This is independent of the type of temperature stratification of the atmospheric boundary layer, either stable or unstable. The sharp increase in the heat exchange coefficient is shown to be associated with increased whitecapping.

Plain Language Summary The heat-moisture ocean-atmosphere exchange, forces acting at the air-water interface, are critical factors determining weather and climate. They are quantified by fluxes, the amounts of heat, moisture, or momentum entering the atmosphere from a unit ocean surface in a unit time. The fluxes are entered directly into atmosphere-ocean circulation models used for climate studies and weather prediction. One of the important questions is the effect of wind waves on air-sea fluxes, especially on the heat exchange, while the largest uncertainties occur at high winds, where reliable data are needed for the prediction of sea storms. This paper describes laboratory experiments in a high-speed wind-wave flume, where the effects of water waves on heat and momentum exchange in the near-water atmospheric boundary layer at high winds were studied. The experiments were conducted in stable atmospheric stratification when water is colder than air. We observed sharp increase in water-air heat transfer correlated with increased whitecapping at wind speeds exceeding 30–35 m/s, similar to that previously observed in experiments at unstable air stratification when the water was warmer than air. The increase in ocean-atmosphere heat transfer caused by the presence of whitecapping may be a mechanism of rapid intensification of ocean storms.

1. Introduction

The correct representation and parameterization of the fluxes of momentum, heat, and moisture are some of the most essential issues in modeling atmosphere and ocean coupling in meteorological and oceanographic research (Jones & Toba, 2001). The turbulent exchange of energy and momentum between ocean surfaces and the atmosphere to a large extent control the energy and water cycle and general circulation of the ocean and atmosphere. At the boundary-layer scale, the turbulent fluxes control the generation of waves and development of the upper ocean mixed layer and atmospheric boundary layer, including conditions of tropical cyclones and storms.

In numerical models of atmosphere and ocean circulation, the air-sea turbulent fluxes of momentum, $\langle u'w' \rangle = u_*^2$, heat $\langle T'w' \rangle = u_* T_*$, and moisture $\langle q'w' \rangle = q_* u_*$ are expressed via formulas through the bulk

parameters of the atmospheric boundary layer measured at a reference level (usually $H_{10} = 10$ m above the water surface): the 10-m wind speed U_{10} , the difference between the 10-m air and water temperature ΔT_{10} , and the difference of relative moisture at the water level and 10 m above the water surface Δq_{10} :

$$\begin{aligned}\langle u'w' \rangle &= C_D U_{10}^2, \\ \langle T'w' \rangle &= C_T U_{10} \Delta T_{10}, \\ \langle q'w' \rangle &= C_E U_{10} \Delta q_{10}.\end{aligned}\quad (1)$$

The dimensionless exchange coefficients, drag coefficient C_D , the Stanton number C_T , and Dalton number C_E all can depend both on wind speed and density stratification of the marine atmospheric boundary layer (MABL) and the effective roughness of the water surface. The heat and moisture transfer coefficients are usually considered equal (Fairall et al., 2003). The validity of this supposition at high winds was recently shown in experiments by Komori et al. (2018). Below, only the Stanton number and drag coefficient will be considered.

According to the Monin-Obukhov similarity theory (Monin & Yaglom, 1965), the vertical profiles of velocity and temperature in a stratified MABL are as follows:

$$u(z) = \frac{u_*}{\kappa} \ln \frac{z}{z_0} + \Phi_m \left(\frac{z}{L} \right), \quad (2)$$

$$T(z) - T(0) = \frac{T_*}{\kappa} \text{Pr}_t \ln \frac{z}{z_{0T}} + \Phi_T \left(\frac{z}{L} \right). \quad (3)$$

Here,

$$L = - \frac{u_*^3}{\kappa \frac{g}{T} \langle T'w' \rangle} \quad (4)$$

is the Monin-Obukhov length scale (Monin & Yaglom, 1965), and Pr_t is the turbulent Prandtl number defined as

$$\text{Pr}_t = \frac{\langle T'w' \rangle \frac{d\langle U \rangle}{dz}}{\langle u'w' \rangle \frac{d\langle T \rangle}{dz}},$$

where z_0 and z_{0T} are the aerodynamic heat roughness heights. The functions $\Phi_m(z/L) = \Phi_T(z/L)$ tend to 0, when $z/L \rightarrow 0$, then following from Equations 2 and 3, the velocity and temperature profiles $u(z)$ and $T(z)$ are logarithmic for $z < L$.

It follows from comparing definitions for the exchange coefficients (Equation 1) with expressions for the velocity (Equation 2) and temperature profiles (Equation 3) that C_D and C_T depend on the characteristics of the stratification of the MABL, defined by the Obukhov scale, and on the properties of the underlying surface parameterized by aerodynamic roughness height. A convenient expression for the latter includes the coefficients of turbulent exchange at neutral stratification:

$$C_{D10N} = \frac{\kappa^2}{(\ln(H_{10}/z_0))^2}, \quad (5)$$

$$C_{T10N} = \frac{\kappa^2}{\text{Pr}_t \ln(H_{10}/z_0) \ln(h_{10}/z_{0T})} = \frac{\kappa \sqrt{C_{D10N}}}{\text{Pr}_t |\ln(H_{10}/z_{0T})|}. \quad (6)$$

Equations 5 and 6 can be regarded as alternative definitions of the aerodynamic roughness parameter z_0 and the temperature roughness z_{0T} .

Parameterization of roughness parameters or the exchange coefficients used in the models of atmospheric circulation is reduced to their dependency on wind speed (Yelland & Taylor, 1996) and in the advanced models (Lykossov, 2002) on the wave age. The problem of dependency of the exchange coefficients in MABL on

wind speed is closely connected with the question of the influence of surface waves and spray, that is, the products of wind-forcing on the exchange of the momentum and mass between the atmosphere and ocean. The effect of waves on the momentum transfer has been studied intensively (see, e.g., Ayet et al., 2020; Husain et al., 2019; Janssen, 1989; Makin et al., 1995; Makin & Mastenbroek, 1996; Makin & Kudryavtsev, 1999; Moon et al., 2004; Takagaki et al., 2012; Takagaki, Komori, & Suzuki, 2016; Takagaki, Komori, Suzuki, et al., 2016; Troitskaya et al., 2012, 2017; Troitskaya, Druzhinin, et al., 2018; Troitskaya, Kandaurov, et al., 2018; Troitskaya & Rybushkina, 2008, and references therein). It has been shown that the momentum transfer by wave disturbances, or the form drag, increases with increasing wind speed due to the widening of the wave spectra. The decrease of the turbulent momentum flux near the water surface leads to the decrease of the wind speed at the standard height and increase of the drag coefficient and the surface aerodynamic roughness parameter.

The influence of wave disturbances on the heat transfer is weaker than on the momentum transfer—at moderate wind speeds, the heat flux controlled by wave-induced disturbances is a fraction of the percentage of the turbulent heat flux (see a discussion of this issue, e.g., in Troitskaya et al., 2013). As a result, the effect of waves on the temperature roughness z_{0T} is practically negligible; the temperature roughness is mostly determined by the molecular transfer and decreases with the increase of the wind friction velocity according to Liu et al. (1979). Then, one can see from Equation 6 that the increase of the heat exchange coefficient $C_{TN10}(U_{10})$ with the increase of the wind speed can be associated only with the increase of the aerodynamic sea surface roughness mainly due to an increase of the waveform drag as assumed by the theoretical models of Makin and Mastenbroek (1996) and Makin (1998).

The experimental data confirm weaker dependence of the heat transfer coefficient C_{T10N} on wind speed compared with $C_{DN10}(U_{10})$ (see Fairall et al., 2003 and Ocampo-Torres et al., 1994), but the character of the dependence is different in different experiments. Several studies (e.g., the algorithm COARE 3.0, Fairall et al., 2003; field data Brut et al., 2005; and laboratory data, Ocampo-Torres et al., 1994) indicate weak growth of C_{T10N} with increasing wind speed U_{10} . Also, a weak dependence of the enthalpy transfer coefficient on the wind speed was found in the recent laboratory experiment by Jeong et al. (2012), who studied heat transfer at the strong wind speeds. Drennan et al. (2007) did not find a dependence of C_{T10N} on wind speed. On the contrary, in a recent work by Komori et al. (2018), a sharp increase in the coefficients of heat and moisture exchange at wind speeds exceeding 35 m/s was experimentally shown, with the aerodynamic resistance coefficient saturated. Komori et al. (2018) explained the observed phenomenon by the effect of wave breaking. In contrast to Makin and Mastenbroek (1996) and Makin (1998), as the simultaneous saturation of the surface drag coefficient and increase of the heat exchange coefficient indicates, the temperature roughness sharply increased with the increase of the air flow velocity. These results indicate that the air-sea heat exchange essentially depends on the thermal properties of the water surface.

The purpose of this study is a detailed experimental investigation of the influence of the small-scale features of water surface disturbances (short waves, wave breakers, whitecaps) on the heat and momentum exchange in the atmospheric boundary layer. We focused specifically on the effect of the water surface disturbances on the heat transfer coefficient, which can be both indirect and direct. The indirect effect comes from the increase of turbulent mixing by the aerodynamic surface roughness and is described by the surface drag coefficient in Equation 6; the direct effect comes from the contribution of the sea surface disturbances to the air-water heat flux and is described by the temperature roughness in Equation 6. Simultaneous measurement of the momentum and heat transfer coefficients allows us to separate the direct and indirect effects and to examine whether the temperature roughness is affected by the water surface disturbances. In addition, contrary to the experiments by Jeong et al. (2012) and Komori et al. (2018), the water temperature was lower than the air temperature. Other differences are the use of artificial wind speed and controlling parameters of waves at certain wind speeds. This helped to describe the dependency of the transfer coefficients on the wind speeds for a wider range of the parameters of the water surface disturbances.

The paper has the following structure. In section 2.1, the experimental setup and a scheme of the adjustment of the aerodynamic surface roughness independent of the wind force are described. Section 2.2 is devoted to a description of the measuring of the transfer coefficients by a profiling method. The method of retrieving 3D spectra of the waves and estimation of the amount of the spray in the boundary layer are described in

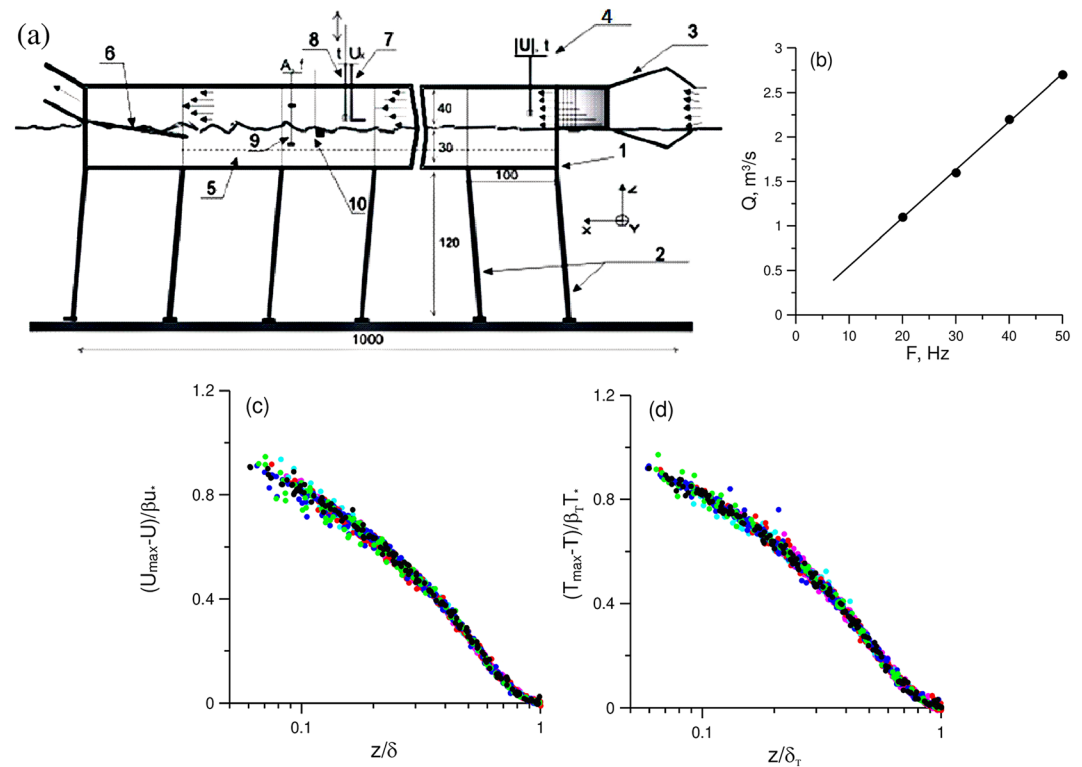


Figure 1. (a) General scheme of the experiments—The embedded measurements are in cm: (1) wind-wave flume body; (2) channel bearings; (3) convergent diffusion section with a honeycomb; (4) hot film anemometer at the entrance; (5) a net along the channel installed at different depths; (6) wave absorber; (7) the Pitot tube on a scanning system; (8) cold film thermometer on the same scanning system; (9) three-channel wire wave-gauge; and (10) a gauge for water temperature measurements. (b) The air volume flux as a function of the fan rotation speed. Dimensionless profiles of the “velocity defect” (c) and the “temperature defect” (d) in self-similar variables (Equations 9 and 20, respectively, for c and d) for the different values of the fan rotation rate. Black symbols correspond to fan speed 20 Hz, green—25 Hz, blue—30 Hz, red—35 Hz, cyan—37 Hz, and magenta—40 Hz.

section 2.3. In sections 3 and 4, the dependency of the transfer coefficients on the parameters of wind flow and the water surface disturbances are presented. The results are discussed in section 5.

2. Methods

2.1. Facility and Equipment

The experiments were carried out in the Thermostratified Wind-Wave Tank (TSWiWaT) of IAP RAS. The detailed description of this experimental facility and the principles of creating and controlling the air flow are given by Troitskaya et al. (2012). The general scheme of the experiments is shown in Figure 1a. The air-flow channel is 10-m length of 0.4×0.4 m cross-section above the water surface. The airflow is created by a centrifugal fan MSB-2-560/80-1850T (produced by Ventur, Sweden). The air flow rate is prescribed by the fan frequency of rotation F ranging from 7.5 to 50 Hz. The airflow velocity at the axis of the channel is proportional to F and varies from 8.8 to 19 m/s, which corresponds to the 10-m wind speed 10–35 m/s (see Figure 1b). To create the temperature stratification of the surface layer of the wind, the air entering the channel was heated to 30–40°C (depending on the air flow rate). The temperature on the water surface in all the experiments was maintained constant at $\sim 15^\circ\text{C}$.

A special feature of this experiment is the ability to control surface waves irrespective of the speed of the wind flow in the channel. For this purpose, a plastic net 0.25 mm thick with a mesh of 1.6×1.6 mm was stretched along the entire channel. The net did not affect the heat exchange but increased substantially the dissipation of the low-frequency part of the wind wave spectra. As a result, the characteristics of surface waves varied depending on the net depth (h_{net}), which varied from 0 (the undisturbed water surface) to 33 cm. Obviously, it produced combinations of wind speeds and wave field patterns that might never exist

Table 1
Parameters of the Experiment (Average Values and 95% Confidence Intervals)

F, s^{-1}	N	h_{net}, cm	$u^*, m/s$	$U_{10}, m/s$	m.s.s.	H_s, m	k_p, m^{-1}	ω_p, s^{-1}	$C_{T10N}(10^{-3})$	$Fr (\%)$
20	2	0	0.43 ± 0.01	13.4 ± 0.1	N/A	N/A	N/A	N/A	0.94 ± 0.09	0
20	1	1.0	0.41	13.1	N/A	N/A	N/A	N/A	0.92	0
20	3	1.5	0.45 ± 0.05	13.4 ± 0.1	0.020	0.74	0.88	33.0	1.07 ± 0.10	0
20	4	3.0	0.50 ± 0.02	13.8 ± 0.3	0.038 ± 0.006	1.4 ± 0.3	0.53 ± 0.2	$24. \pm 4$	1.15 ± 0.03	0.005 ± 0.006
20	1	4.5	0.51	13.9	0.042	1.6	0.43	22.	1.15	0.037
20	3	6.0	0.50 ± 0.02	13.8 ± 0.2	0.044 ± 0.01	1.8 ± 0.2	0.41 ± 0.2	$22. \pm 1$	1.15 ± 0.11	0.052 ± 0.036
20	1	9.0	0.49	13.9	0.040	1.7	0.41	22.	1.12	0.032
20	1	33.	0.50	13.9	0.045	1.9	0.40	22.	1.11	0.066
25	2	0.	0.55 ± 0.2	17.0 ± 0.1	N/A	N/A	N/A	N/A	0.92 ± 0.03	0
25	2	1.5	0.64 ± 0.2	17.7 ± 0.1	0.020 ± 0.002	0.79 ± 0.03	0.87 ± 0.05	34.0 ± 3	1.10 ± 0.08	0
25	3	3.0	0.72 ± 0.06	18.7 ± 0.9	0.04 ± 0.01	1.4 ± 0.3	0.46 ± 0.05	22.0 ± 2	1.14 ± 0.04	0.027 ± 0.023
25	3	4.5	0.79 ± 0.06	18.9 ± 0.9	0.05 ± 0.01	2.0 ± 0.3	0.36 ± 0.05	19.4 ± 0.6	1.133 ± 0.12	0.14 ± 0.13
25	2	6.0	0.70 ± 0.06	18.6 ± 0.6	0.06 ± 0.0006	2.5 ± 0.2	0.31 ± 0.02	18.6 ± 0.5	1.11 ± 0.01	0.50 ± 0.15
25	2	33.	0.67 ± 0.003	18.4 ± 0.2	0.07 ± 0.01	3.0 ± 0.3	0.28 ± 0.02	17.9 ± 1.0	1.03 ± 0.02	0.95 ± 0.32
30	2	0.	0.74 ± 0.01	21.6 ± 0.4	N/A	N/A	N/A	N/A	0.92 ± 0.02	0
30	3	1.5	0.82 ± 0.04	22.1 ± 0.3	0.03 ± 0.02	0.95 ± 0.5	0.8 ± 0.3	$32. \pm 3.$	1.03 ± 0.04	0
30	7	3.0	0.91 ± 0.06	23.1 ± 0.6	0.05 ± 0.02	1.7 ± 0.6	0.41 ± 0.02	20.3 ± 0.9	1.11 ± 0.06	0.17 ± 0.23
30	3	4.5	1.00 ± 0.1	$24. \pm 1.$	0.07 ± 0.02	2.8 ± 0.9	0.30 ± 0.07	18.0 ± 3	1.16 ± 0.01	0.64 ± 0.71
30	4	6.	0.93 ± 0.09	23.4 ± 1.0	0.08 ± 0.01	3.5 ± 0.1	0.24 ± 0.01	$16.5 \pm 3.$	1.03 ± 0.11	1.59 ± 0.34
30	2	9.	0.93 ± 0.01	23.5 ± 0.2	0.09 ± 0.02	4.1 ± 0.2	0.22 ± 0.04	15.6 ± 0.04	1.0 ± 0.2	2.59 ± 0.56
30	2	18.	0.89 ± 0.08	23.1 ± 0.5	0.09 ± 0.01	4.2 ± 0.3	0.21 ± 0.01	15.8 ± 0.5	0.96 ± 0.13	2.92 ± 0.06
30	1	33.	0.95	23.5	0.085	4.4	0.2	15.5	1.0	2.70
35	1	0.	0.98	26.35	N/A	N/A	N/A	N/A	0.97	0
35	2	1.5	1.10 ± 0.1	27.8 ± 0.6	0.041 ± 0.006	1.6 ± 0.6	0.4 ± 0.1	$20. \pm 5.$	1.04 ± 0.07	0.03 ± 0.04
35	3	3.	1.20 ± 0.1	$29. \pm 1.$	0.055 ± 0.001	3.0 ± 0.1	0.21 ± 0.02	$15. \pm 2.$	1.10 ± 0.08	0.56 ± 0.07
35	2	4.5	1.26 ± 0.01	29.5 ± 0.2	0.070 ± 0.01	3.9 ± 0.6	0.18 ± 0.01	$14. \pm 1.$	1.08 ± 0.03	1.5 ± 1.0
35	2	5.	1.29 ± 0.01	29.8 ± 0.2	0.076 ± 0.002	4.2 ± 0.01	0.18 ± 0.01	13.9 ± 0.3	1.10 ± 0.22	1.70 ± 0.25
35	3	6.	1.29 ± 0.03	29.8 ± 0.3	0.085 ± 0.003	4.8 ± 0.06	0.17 ± 0.01	13.8 ± 0.6	1.08 ± 0.02	2.45 ± 0.5
35	2	9.	1.33 ± 0.03	30.2 ± 0.3	0.10 ± 0.003	5.9 ± 0.3	0.155 ± 0.01	12.9 ± 0.8	1.09 ± 0.16	3.68 ± 0.11
35	3	12.	1.36 ± 0.02	30.4 ± 0.7	0.10 ± 0.008	6.0 ± 0.3	0.15 ± 0.01	13.0 ± 0.5	1.27 ± 0.11	4.08 ± 0.16
35	1	33.	1.37	30.5	0.10	6.2	0.12	12.8	1.12	4.21
37	1	0.	1.14	29.1	N/A	N/A	N/A	N/A	1.01	0
37	1	1.5	1.25	30.2	0.04	1.9	0.33	17.2	1.07	0.10
37	2	3.	1.39 ± 0.09	31.7 ± 0.8	0.054 ± 0.001	3.1 ± 0.3	0.19 ± 0.01	14.1 ± 0.5	1.11 ± 0.02	0.96 ± 0.08
37	2	4.5	1.42 ± 0.02	32.1 ± 0.2	0.070 ± 0.005	4.1 ± 0.1	0.17 ± 0.01	13.5 ± 0.4	1.08 ± 0.21	1.9 ± 0.6
37	2	6.	1.45 ± 0.05	32.2 ± 0.3	0.08 ± 0.01	4.7 ± 0.2	0.17 ± 0.01	13.5 ± 0.3	1.14 ± 0.01	2.6 ± 0.8
37	1	7.5	1.48	32.4	0.09	5.4	0.15	12.7	1.22	3.11
37	2	9.	1.50 ± 0.06	32.7 ± 0.3	0.10 ± 0.02	5.8 ± 0.5	0.15 ± 0.01	$13. \pm 1.$	1.23 ± 0.12	3.7 ± 1.0
37	1	10	1.50	32.6	0.11	6.1	0.15	13.3	1.32	4.23
40	2	0.	1.32 ± 0.03	32.4 ± 0.1	0.03 ± 0.02	1.1 ± 0.2	0.9 ± 0.3	25.5 ± 2	1.00 ± 0.08	0
40	2	1.5	1.44 ± 0.01	33.8 ± 0.3	0.05 ± 0.01	2.6 ± 0.5	0.23 ± 0.02	15.7 ± 0.5	0.99 ± 0.12	0.6 ± 0.5
40	2	2.5	1.58 ± 0.01	35.1 ± 0.1	0.060 ± 0.001	3.5 ± 0.2	0.17 ± 0.005	13.0 ± 0.5	1.13 ± 0.01	1.66 ± 0.05
40	3	3.	1.61 ± 0.07	35.3 ± 0.5	0.066 ± 0.009	3.7 ± 0.4	0.17 ± 0.02	13.1 ± 0.4	1.18 ± 0.05	2.0 ± 0.3
40	2	4.	1.68 ± 0.05	35.6 ± 0.9	0.074 ± 0.01	4.0 ± 0.5	0.16 ± 0.01	13.0 ± 0.04	1.25 ± 0.04	2.5 ± 0.7
40	3	4.5	1.68 ± 0.08	35.8 ± 0.3	0.078 ± 0.01	4.5 ± 0.5	0.15 ± 0.01	12.6 ± 0.5	1.24 ± 0.13	2.6 ± 0.2
40	2	5	1.71 ± 0.03	35.7 ± 0.7	0.080 ± 0.01	4.7 ± 0.1	0.15 ± 0.01	12.6 ± 0.7	1.30 ± 0.01	2.9 ± 0.2
40	2	6	1.73 ± 0.03	35.9 ± 0.1	0.083 ± 0.001	5.0 ± 0.1	0.143 ± 0.005	12.7 ± 0.4	1.30 ± 0.01	2.8 ± 0.5
40	1	9	1.73	36.4	0.10	6.4	0.14	12.6	1.56	4.0
40	2	12	1.68 ± 0.01	36.6 ± 0.02	0.108 ± 0.009	6.7 ± 0.4	0.13 ± 0.001	12.1 ± 0.4	1.78 ± 0.25	4.28 ± 0.03
40	1	33	1.58	36.5	0.111	7.5	0.12	11.6	1.99	0

Note. F is the fan frequency, N is the number of experimental runs, h_{net} is the depth of the net, u^* is the friction velocity, U_{10} is the 10-m wind speed, m.s.s. is the mean square slope of the wave field, H_s is significant wave height, k_p and ω_p are the peak wavenumber and frequency of the wind wave spectra, C_{T10N} is the Stanton number, and Fr is the probability of wave breaking Equation 30. The drag coefficient C_{D10N} can be calculated using Equation 19; the parameter of the temperature roughness Equation 28 can be found in Equation 29 by C_{D10N} and C_{T10N} .

in deep water. At the same time, this technique allows to directly investigate the effect of geometric roughness of the water surface on the wind flow. The waves were strongly suppressed at $h_{net} = 0$; at $h_{net} = 33$ cm, the net had practically no effect on the parameters of the waves for all wind speeds under consideration. It should be emphasized that, at a given rotation speed of the fan F (Table 1), setting the

net at different depths changed not only the wave field but also the wind speed. However, the correlation of the fan rotation speed with the wind friction velocity (coefficient of determination 0.92 from the data of Table 1) is much higher, than with the wave height (coefficient of determination 0.40).

Velocity and temperature profiles in the working section of the flume (6.5 m from the entrance channel) were measured simultaneously by the Pitot tube and hot film gauge installed on the vertical scanner, respectively. The L-shaped Pitot tube with a differential pressure transducer (Baratron MKS 226 A) provided an accuracy of velocity measurement of 3 cm/s. The accuracy of temperature measurements with the hot film was 0.1°C. The velocity and temperature profiles were measured by a scanning method with the height step 3–5 mm and the data accumulating 2 min at each point. For each fixed wind and depth of the net parameters, two profiles of velocity and temperature were measured for subsequent averaging. The lower level of scanning was located 1 cm above the wave crests and depended on the wind speed, whereas the upper layer was 38 cm (2 cm below the ceiling of the channel). The temperature and wind speed at the inlet of the flume were controlled with the additional hot film gauge. The temperature gauge was also positioned under the water in the working section to measure the temperature of the water surface layer.

The wind-wave field parameters in the flume were measured by an array of three-wire gauges positioned in the corners of an equilateral triangle (2.5-cm sides); the data sampling rate was 100 Hz.

2.2. The Retrieval of the Parameters of the Air Boundary Layer

2.2.1. The Retrieval of the Momentum Flux and Aerodynamic Roughness

To determine the parameters of the atmospheric boundary layer in our previous experiments (Troitskaya et al., 2012), we used an algorithm that generalizes the model of the boundary layer near a flat surface following Coles (1956). It is well known that the boundary layer on a smooth flat plate is composed of the viscous sublayer having a thickness of about $\delta_{vis} = \nu_a/u_*$ (less than 0.1 cm), positioned above the layer of constant fluxes having a thickness of about 0.15δ , where δ is the boundary layer displacement thickness. The “wake” part of the turbulent boundary layer was located higher up on the border of the displacement layer. In a turbulent boundary layer over a waved surface, an additional layer is generated, in which there is a transfer of momentum from the airflow to the wave perturbations on the water surface and the sum of turbulent and wave momentum fluxes is constant:

$$\tau_{turb}(z) + \tau_{wave}(z) = \rho_a u_*^2, \quad (7)$$

where ρ_a is the air density and $\tau_{wave}(z)$ decreases with increasing distance from the boundary on a scale of the wave turbulent boundary layer $h_{wave} \sim \sqrt{\nu_t(h_{wave})/k(V_p - U(h_{wave}))}$, which, according to Belcher et al. (1993), can be determined from the following relationship:

$$kh_{wave} \left(\frac{\kappa V_p}{u_*} + \ln k z_0 - \ln h_{wave} k \right) = \kappa^2, \quad (8)$$

where V_p and k are the phase velocities and the wave number corresponding to the frequency of the peak of the elevation surface spectrum, respectively. The numerical values of the parameters of wind and waves in the flume (that are obtained as shown below) give an estimate of $kh_{wave} \sim 0.1$ (see also Makin et al., 1995). Here, the condition $h_{wave} < 0.15\delta$ is observed, and within the layer of the constant momentum flux, there is a layer of constant turbulent momentum flux $\tau_{turb}(z) = \rho_a u_*^2$, in which the velocity depends on the vertical coordinate (logarithmically). As a rule, in wind tunnels and wind-wave flumes, the thickness of the layer of constant fluxes is very small; for example, in our flume, it was ~ 3 cm. The measurement of the wind speed and temperature at such a small distance from the surface of the waved water surface (especially at strong winds) is difficult, mainly due to the effect of spray from the wave crests. The approach of Troitskaya et al. (2012) was based on the property of self-similarity of the profiles of velocity defect in the near-wall turbulent flows (see Figure 1c):

$$\frac{U_{max} - U(z)}{u_*} = F\left(\frac{z}{\delta}\right), \quad (9)$$

where U_{max} is the maximum velocity in a turbulent boundary layer.

Here we apply an alternative approach based on the use of integral quantities in the boundary layer described by Abramovich (1969). As will be shown below, the obtained boundary layer parameters are close to those yielded by the approach by Troitskaya et al. (2012).

The equation of balance of the horizontal component of the momentum in the boundary layer can be derived from the equation of the turbulent boundary layer:

$$U \frac{\partial U}{\partial x} + W \frac{\partial U}{\partial z} - U_{\max} \frac{dU_{\max}}{dx} = \frac{\partial \langle U'W' \rangle}{\partial z} \quad (10)$$

and using the condition of incompressibility

$$\frac{\partial U}{\partial x} + \frac{\partial W}{\partial z} = 0 \quad (11)$$

Identical transformations of Equation 10 with the use of Equation 11 give

$$U \frac{\partial (U - U_{\max})}{\partial x} + W \frac{\partial (U - U_{\max})}{\partial z} + (U - U_{\max}) \frac{dU_{\max}}{dx} = - \frac{\partial \langle U'W' \rangle}{\partial z}. \quad (12)$$

Integration of Equation 12 from the water surface to the thickness of the boundary layer δ yields

$$\begin{aligned} \frac{d}{dx} \int_0^\delta U(U - U_{\max}) dz - U(U - U_{\max})|_{z=\delta} \frac{d\delta}{dx} + W(U - U_{\max})|_{z=\delta} + \frac{dU_{\max}}{dx} \int_0^\delta (U - U_{\max}) dz = \\ = (\langle U'W' \rangle + W(U - U_{\max}))|_{z=0}. \end{aligned} \quad (13)$$

This equation coincides with the balanced equation for the horizontal component of the momentum in the boundary layer, derived in the textbook of Abramovich (1969) with the use of an alternative approach. He used convenient notations where

$$\delta_* = \int_0^\delta \left(1 - \frac{U(z)}{U_{\max}} \right) dz - \quad (14)$$

is the boundary layer displacement thickness and

$$\delta_{**} = \int_0^\delta \left(1 - \frac{U(z)}{U_{\max}} \right) \frac{U(z)}{U_{\max}} dz - \quad (15)$$

is the boundary layer momentum thickness.

The second and the third terms in the left-hand side of Equation 13 are zero, because $U(\delta) = U_{\max}$. We also consider that the right-hand side of Equation 13 is the sum of two terms. The first one is the turbulent momentum flux divided by ρ_a . The second term is the momentum flux associated with the turbulent-averaged flow and is also divided by ρ_a . At the water surface, it is determined by the wave disturbances induced in the air flow by the waves at the water surface. The sum of these two terms is equal to u_*^2 according to Equation 7. Taking this into account (Equation 13), it can be written as

$$u_*^2 = \frac{d(U_{\max}^2 \delta_{**})}{dx} + \frac{\delta_* dU_{\max}^2}{2 dx}. \quad (16)$$

The advantage of the integral method for retrieving the parameters of a turbulent boundary layer is its robustness compared to the profiling method used by Troitskaya et al. (2012). The main source of errors in the profile method is the uncertainty in determining the boundary layer thickness, δ , that is determined from the approximation of the velocity profile in the “wake” part of the boundary layer. This value depends on the choice of the interval, over which the approximation is performed, especially with noticeable errors in the velocity measurements that are always present in turbulent flows. Also, the uncertainty in δ , the upper

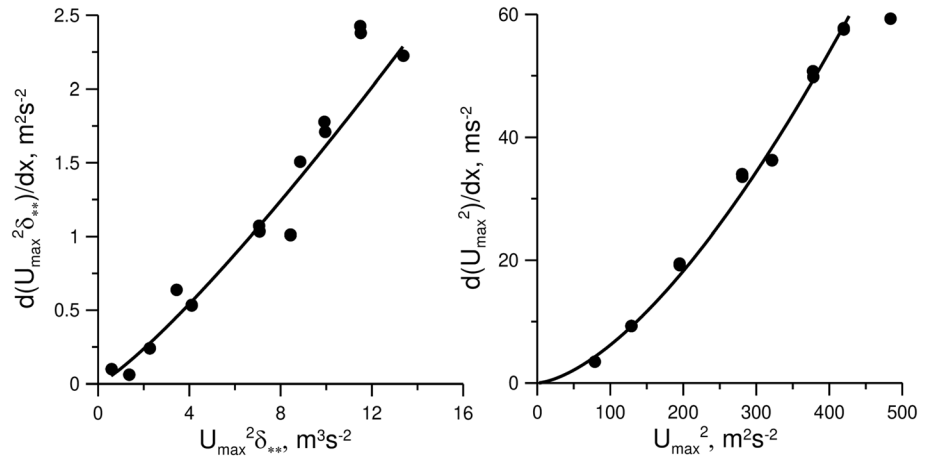


Figure 2. The auxiliary calibration curves retrieving u_*^2 . Points are the experimental data and curves are the power approximations.

limit in Equations 14 and 15, only slightly affects the values of the integrals, since the integrand near the upper limit of integration is close to zero. Large number of data points are required, including close to the water surface, for statistically significant differences in the boundary layer parameters created by different net depths (Zavadsky & Shemer, 2012). Such thorough measurements were impossible due to large amount of spray at the high winds used in our experiments. That is why we used the integral method instead of the profiling one.

To determine the dynamic velocity from Equation 16, special series of measurements were carried out in which the velocity profiles were measured in different sections of the channel at 4.5 m (fifth section), 6.5 m (seventh section), and 7.5 m (eighth section). To calculate the integrals in Equations 14 and 15, values of the flow velocity up to $z = 0$ are required. Since measurements at such distances from the surface were not performed, extrapolation of the velocity profiles in the integrands of Equations 14 and 15 took into account the self-similarity of the velocity defect profile Equation 9. The approximation of the velocity profile $U(z)$ in Equation 9 was as in Troitskaya et al. (2012):

$$U(z) = U_{\max} + \begin{cases} \left(-\frac{u_*}{\kappa} \ln(z/\delta) + \alpha \right); & z/\delta < 0.15 \\ -\beta u_* (1 - z/\delta)^2; & z/\delta > 0.15 \end{cases} \quad (17)$$

The parameters U_{\max} , β , and δ were retrieved from the second-order polynomial approximation of the measured velocity profile. The parameters α and β were calculated from the smooth matching of the logarithmic function with the polynomial approximation of the velocity profile at $z/\delta = 0.15$ and the condition $U(z_0) = 0$ at a certain $z_0 \ll 0.15\delta$. Here, $z_0 = 0.1$ mm was chosen. The dependence of the integrals in Equations 14 and 15 on this choice was weak (no more than 5% when z_0 changed by an order of magnitude) because the thickness of the constant flow layer is a small part of the thickness of the boundary layer. Using the constructed approximations, the integrals in Equations 14 and 15 were calculated as were the derivatives included in Equation 16. Figure 2 shows the calibration curves for this laboratory setup, which were used to determine the friction velocity. The calibration curves were approximated by power functions

$$\begin{aligned} \frac{d(U_{\max}^2 \delta_{**})}{dx} &= A_1 (U_{\max}^2 \delta_{**})^{m_1}, \\ \frac{dU_{\max}^2}{dx} &= A_2 (U_{\max}^2)^{m_2}. \end{aligned}$$

Here $A_1 = \exp(-2.3 \pm 0.4)$, $m_1 = 1.2 \pm 0.2$, $A_2 = \exp(-5.4 \pm 0.6)$, and $m_2 = 1.6 \pm 0.1$, with the velocity expressed in m/s and the sizes in m. The standard error of the regression u_*^2 is $\sim 0.2 \text{ m}^2 \text{ s}^{-2}$. Using the obtained calibration curves, the friction velocity can be retrieved using Equation 16 from the measured velocity

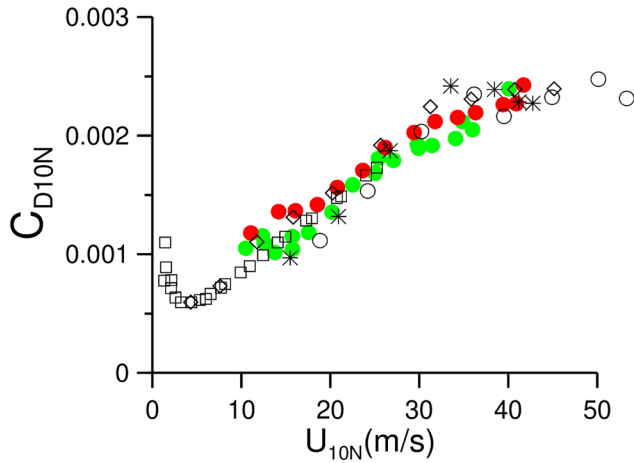


Figure 3. Comparison of $C_{D10}(U_{10})$ obtained by the integral method (red circles) and the profiling method in Troitskaya et al. (2012) (green circles). The open symbols and the asterisks are the data of Donelan et al. (2004).

profiles in one section. To find the roughness parameter in the logarithmic velocity profile in the layer of constant fluxes we used:

$$U(z) = \frac{u_*}{\kappa} \ln\left(\frac{z}{z_0}\right)$$

where the value of the air flow velocity, $U(z_*)$, at the upper boundary of the layer of constant fluxes, $z_* = 0.15\delta$. The value $U(z_*)$ was either directly measured (if the wave crests were below z_*) or extrapolated following the polynomial approximation of the airflow velocity profile measured in the “wake” part of the boundary layer. Then the equivalent wind speed at an arbitrary height z is

$$U(z) = \frac{u_*}{\kappa} \ln\left(\frac{z}{z_*}\right) + U(z_*). \quad (18)$$

The 10-m air flow velocity U_{10} was calculated at the standard height $z = H_{10} = 10$ m using Equation 18, and the drag coefficient of the water surface was

$$C_{D10} = \frac{u_*^2}{U_{10}^2}. \quad (19)$$

The dependence $C_{D10}(U_{10})$ obtained using this integral method is compared in Figure 3 with the dependence obtained in Troitskaya et al. (2012) using the profiling method—both methods give similar results. Both data sets are in close agreement with the data of Donelan et al. (2004).

2.2.2. Retrieving of the Heat Flux and the Temperature Roughness

A similar integral method was used to retrieve the values of the heat transfer coefficient and temperature roughness from the measured velocity and temperature profiles in the channel. As for the velocity, the profile of the temperature defect is self-similar (see Figure 1d):

$$\frac{\Delta T_{\max} - \Delta T(z)}{\beta_T T_*} = G\left(\frac{z}{\delta_T}\right). \quad (20)$$

Here $\Delta T(z) = T(z) - T(0)$, $\Delta T_{\max} = T_{\max} - T(0)$, and $T(0)$ is the water surface temperature.

For the approximation of the self-similar dependence for the profile of the temperature defect, we used an expression similar to Equation 17:

$$\Delta T_{\max} - \Delta T(z) = \begin{cases} T_* \left(\frac{1}{\kappa} - \text{Pr}_t \ln(z/\delta_T) + \alpha_T \right); & z/\delta_T < 0.15 \\ \beta_T T_* (1 - z/\delta_T)^2; & z/\delta_T > 0.15 \end{cases}.$$

The turbulent Prandtl number Pr_t was taken as 0.85 following Zilitinkevich (1987). This value was also confirmed by direct numerical simulation of the turbulent boundary layer above the waved water surface following Druzhinin et al. (2015).

The integral equations of heat balance in a stratified boundary layer were derived from the stationary differential equation for the temperature averaged over turbulent pulsations, which can be written as

$$U \frac{\partial(\Delta T - \Delta T_{\max})}{\partial x} + W \frac{\partial(\Delta T - \Delta T_{\max})}{\partial z} = - \frac{\partial \langle T' W' \rangle}{\partial z}.$$

Given the incompressibility condition, this equation transforms into the divergent form

$$\frac{\partial U(\Delta T - \Delta T_{\max})}{\partial x} + \frac{\partial W(\Delta T - \Delta T_{\max})}{\partial z} = - \frac{\partial \langle T' W' \rangle}{\partial z}.$$

Integrating this equation from the surface of the water to the boundary layer thickness, δ , gives

$$\begin{aligned} \frac{d}{dx} \int_0^{\delta} U(\Delta T - \Delta T_{\max}) dz - U(\Delta T - \Delta T_{\max})|_{z=\delta} \frac{d\delta}{dx} + W(\Delta T - \Delta T_{\max})|_{z=\delta} = \\ = (\langle T'W' \rangle + W(\Delta T - \Delta T_{\max}))|_{z=0}. \end{aligned} \quad (21)$$

We take into account that the gas temperature at the upper boundary of the boundary layer is equal to the unperturbed one and the right-hand side of Equation 21 is the total heat flux equal to the sum of the turbulent ($\tau_{\text{turb}}^T(z)$) and wave ($\tau_{\text{wave}}^T(z)$) heat fluxes, similar to Equation 7:

$$\tau_{\text{turb}}^T(z) + \tau_{\text{wave}}^T(z) = u_* T_*,$$

introducing the notation

$$\delta_{***} = \int_0^{\delta_T} \frac{U}{U_{\max}} \left(\frac{\Delta T}{\Delta T_{\max}} - 1 \right) dz, \quad (22)$$

which yields for Equation 21

$$u_* T_* = \frac{d(U_{\max} \Delta T_{\max} \delta_{***})}{dx}. \quad (23)$$

Integrating Equation 23 over x from the entrance to the canal to the seventh working section, located at a distance of $L_7 = 6.5$ m, gives the average value of the heat flux on the water surface as follows:

$$u_* T_* = \frac{(U_{\max} \Delta T_{\max} \delta_{***})|_{x=L_7}}{L_7}. \quad (24)$$

The derivation of Equation 24 assumes that homogeneous gas (air) with the constant temperature enters the channel inlet, so that $\Delta T = \Delta T_{\max}$, and as a result, $\delta_{***}|_{x=0} = 0$. When calculating the integral 22, the extrapolation of the velocity and temperature profiles was similar to that used in the calculation of the integrals in Equations 14 and 15.

To determine the temperature roughness parameter in the logarithmic part of the temperature profile in the layer of constant fluxes we used,

$$\Delta T(z) = \frac{T_*}{\kappa} \text{Pr} \ln \left(\frac{z}{z_{0T}} \right), \quad (25)$$

that is, the same approach that we used to calculate the aerodynamic roughness parameter. Then the temperature difference between a certain level z and the water surface was

$$\Delta T(z) = \frac{T_*}{\kappa} \text{Pr} \ln \left(\frac{z}{z_{T*}} \right) + \Delta T(z_{T*}), \quad (26)$$

where $z_{T*} = 0.15\delta_T$ and $\Delta T(z_{T*})$ are the temperature difference between the level z_{T*} and the water surface—which was either directly measured, if the wave crests were below z_{T*} , or extrapolated following the polynomial approximation of the temperature profile measured in the “wake” part of the boundary layer.

Using Equation 26 for calculating the temperature difference between the surface water and air at a standard height $H_{10} = 10$ m and Equation 18 for U_{10} gives then the Stanton number:

$$C_{T10N} = \frac{u_* T_*}{U_{10} \Delta T_{10}}. \quad (27)$$

It follows directly from Equation 25 that

$$\frac{T_*}{\Delta T(H_{10})} = \frac{\kappa}{\text{Pr} \ln \left(\frac{H_{10}}{z_{0T}} \right)}, \quad (28)$$

which depends only on temperature roughness. The dimensionless parameter (Equation 28) is usually used instead of the dimensional temperature roughness.

Comparing Equations 19, 27, and 28 easily gives

$$C_{T10N} = \frac{T_*}{\Delta T(H_{10})} \sqrt{C_{D10N}}. \quad (29)$$

Equation 29 is useful for the analysis of the dependency of the Stanton number, the parameter of temperature roughness, and the coefficient of resistance of the wind and waves.

2.3. Quantifying Characteristics of the Disturbed Water Surface

Three-dimensional, space-time spectra were obtained from the measured elevations of the water surface in three points using Fourier directional method (FDM) described in detail by Troitskaya et al. (2012). The FDM is akin to wavelet directional method (WDM), suggested by Donelan et al. (1996).

Also, the simultaneous measurement of water elevation $\eta(x, y, t)$ at three close points (x_1, y_1) , (x_2, y_2) , and (x_3, y_3) enabled us to retrieve the two components of the slope of water surface, ξ_x and ξ_y , by the following equations:

$$\begin{aligned} \xi_x &= (\Delta y_{1,3} - \Delta y_{1,2}) / \Delta, \\ \xi_y &= (\Delta y_{1,2} - \Delta y_{1,3}) / \Delta, \\ \Delta &= \Delta x_{1,2} \Delta y_{1,3} - \Delta x_{1,3} \Delta y_{1,2}, \end{aligned}$$

and to construct the two-dimensional slope probability density function (PDF) of the water surface $P(\xi_x, \xi_y)$. Using the slope PDF, one can find the mean-square slope (m.s.s.) of the water surface:

$$m.s.s. = \int_{-\infty}^{\infty} \int_{-\infty}^{\infty} (\xi_x^2 + \xi_y^2) P(\xi_x, \xi_y) d\xi_x d\xi_y.$$

The function $P(\xi_x, \xi_y)$ was used to quantify the intensity of the wave breaking as a probability of exceeding the threshold angle $\theta_{br} = 30.37^\circ$ (see Longuet-Higgins & Smith, 1983):

$$Fr = \iint_{\sqrt{\xi_x^2 + \xi_y^2} > \tan \theta_{br}} P(\xi_x, \xi_y) d\xi_x d\xi_y. \quad (30)$$

The parameters of the air flow (friction velocity and 10-m wind speed), the characteristics of the wave field (significant wave height, m.s.s., and the peak wave number and frequency of the surface wave spectrum), the control parameters of the experiment (the fan rotation rate and control net depth), and the number of experimental runs for each set of the parameters are given in Table 1.

We discuss the characteristics of the wave field. Figures 4a and 4b show the dependence of the wave number of the surface wave spectral peak, k_p , on the significant wave height (SWH) H_s . One can see that for all experiments, k_p is proportional to H_s (Figure 4a), and their product is approximately constant and equal ~ 0.18 (Figure 4b). This indicates saturation of the wave field, which means that the shape of the dominant waves is approximately the same at different wind speeds.

The m.s.s. of the waved water surface, calculated over the entire spectrum of waves (Figure 4c), increases with increasing wave height. This assumes an increase in the width of the spectrum of surface waves with increasing heights of surface waves. The dependence of the probability of wave breaking on the significant wave height, shown in Figure 4d, has a threshold. Intense breakings begin when H_s exceeds 2 cm, which corresponds to m.s.s. exceeding 0.04 ± 0.01 according to Figure 4c. These properties and characteristics of the wave field will be used below to interpret the peculiarities of the coefficients of heat and momentum exchange between water and air.

3. Experimental Dependencies of the Turbulent Exchange Coefficients on Wind Velocity

Figure 5c presents the value $T_*/\Delta T_{10}$ where $\Delta T_{10} = T(H_{10}) - T_w$. According to Equation 28, $T_*/\Delta T_{10}$ is connected by functional dependence with the temperature roughness height, then the phrase “the logarithm of the temperature roughness” is sometimes used as the definition of this value. It can be seen from Figure 5a that C_{D10} increases with the increase of u_* , and the values obtained for different parameters of the waves and

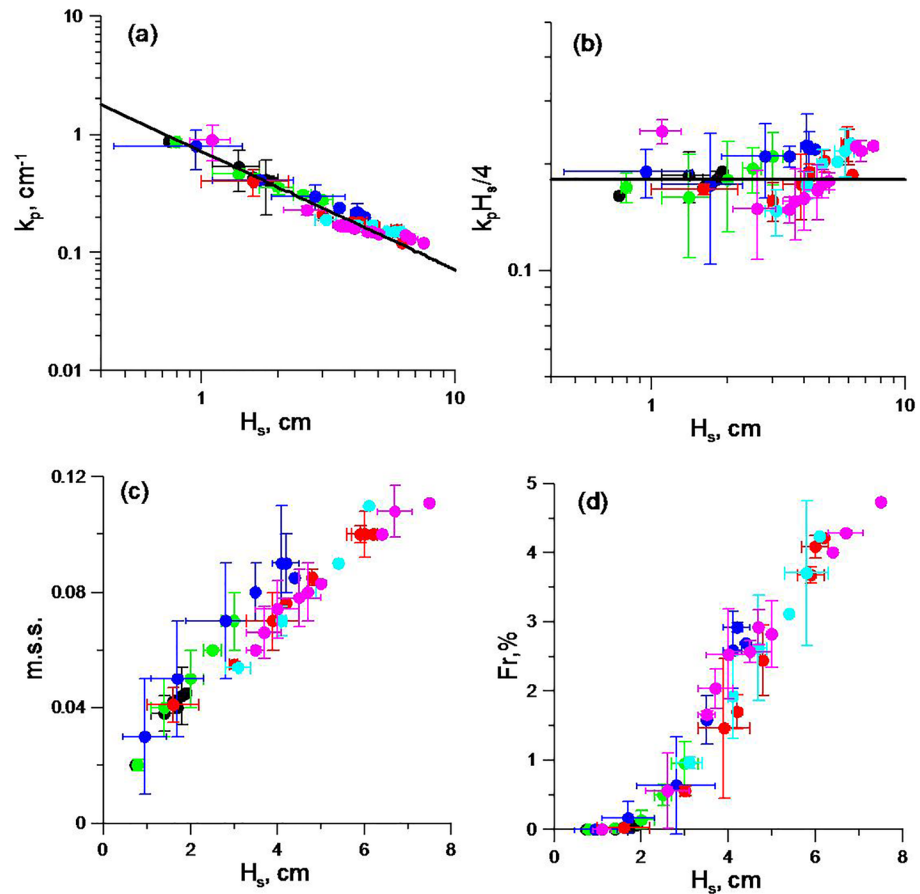


Figure 4. The peak wave numbers in the wind wave spectra (the solid line is $\sim H_s^{-1}$) (a) and the mean slope of the dominant wave (b) versus the significant wave height. The mean square slope of the wave field (m.s.s.) via significant wave height (c) and the probability of breaking occurrence via significant wave height (d). Black symbols correspond to fan speed 20 Hz, green—25 Hz, blue—30 Hz, red—35 Hz, cyan—37 Hz, and magenta—40 Hz.

air flow within the experimental error collapse into one curve. The resulting dependence is very close to that shown by Donelan et al. (2004). Noteworthy, the data agree with field data by Powell et al. (2003) and French et al. (2007) when they are expressed via the friction velocity. This means that the parameters of the surface disturbances, which determine the spreading of the exchange coefficients at a certain wind velocity, are parameterized mostly by the friction velocity or turbulent stress, which presents the forcing acting at the water surface.

It follows from Figure 5b that for $u_* < 1.5$ m/s (corresponding to $U_{10} \approx 33$ –35 m/s according to Figure 5d and Table 1), the Stanton number is almost constant and equal to approximately 0.0011, and this result is in good agreement with the data of Jeong et al. (2012). The constant C_{T10N} accompanied by the increase C_{D10N} following Equation 29 is ensured by the decreasing dependence of $\frac{T_*}{\Delta T(H_{10})}$ on u_* ; see Figure 5c. One can see that for $u_* < 1.5$ m/s, this dependence agrees well with the model of temperature roughness of the air flow above the water surface proposed by Liu et al. (1979). According to this model, the heat transfer at the air-water interface is due to molecular transfer, and

$$\Delta T(z) = T_* \left(2.18 \ln \frac{zu_*}{\nu_a} + 3.8 \right), \quad (31)$$

where ν_a is the air kinematic viscosity. However, we note that at $u_* > 1.5$ m/s the Stanton number and the temperature roughness sharply increase. A similar increase of the Stanton number was observed in the experiments by Komori et al. (2018), who explained it by an effect of wave breaking (see also Figure 5c).

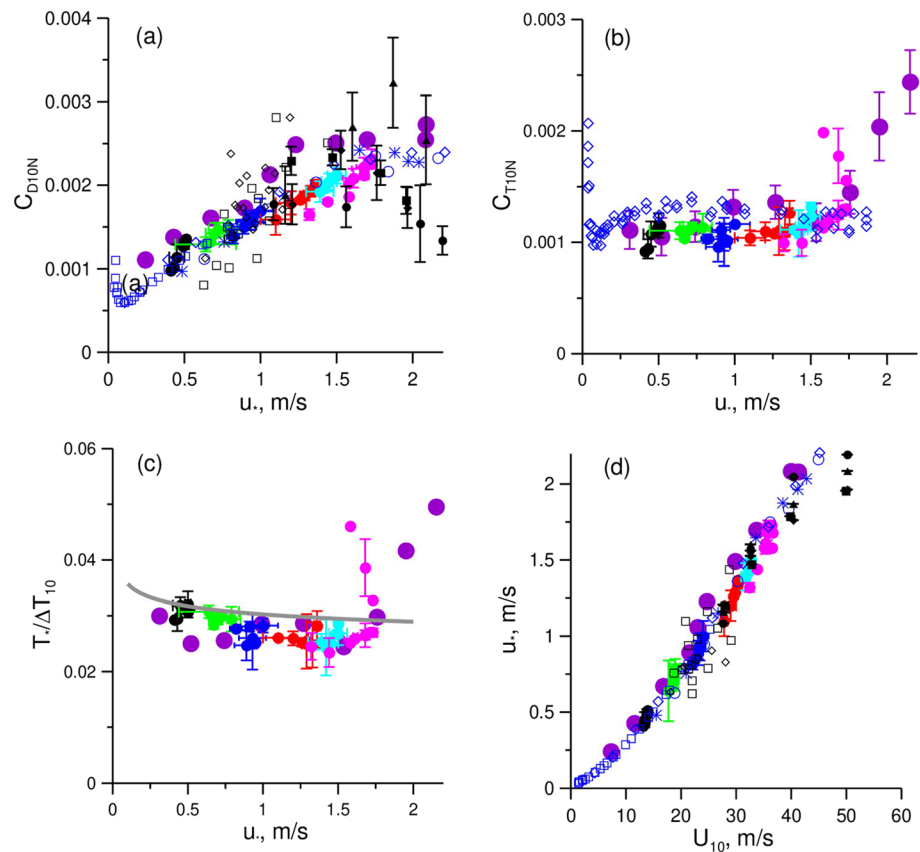


Figure 5. Dependencies on u^* of drag coefficient C_{D10N} (a), the open black symbols are the data by French et al. (2007); heat transfer coefficient C_{T10N} (b); parameter of the temperature roughness (c); and u^* as a function of U_{10} (d). The gray curve in panel (c) is given by Equation 31. In panels (a) and (d), the blue open symbols are data of Donelan et al. (2004) and the filled black symbols are data of Powell et al. (2003). In panel (b), the blue open symbols are data of Jeong et al. (2012). In all panels, the colors follow Figure 4; the violet circles are data from Takagaki et al. (2012) and Komori et al. (2018).

Note that the values of the exchange coefficients and the temperature roughness obtained by Komori et al. (2018) noticeably exceed that of the present data (see Figures 5a–5c). This can be explained by the dependence of these values on the wave fetch and is shown in Figure 6, which shows the similar decreasing dependency of C_{D10N} , C_{T10N} , and $T^*/\Delta T_{10}$ on the wave age parameter c_p/u^* obtained both by Komori et al. (2018) and in the present study.

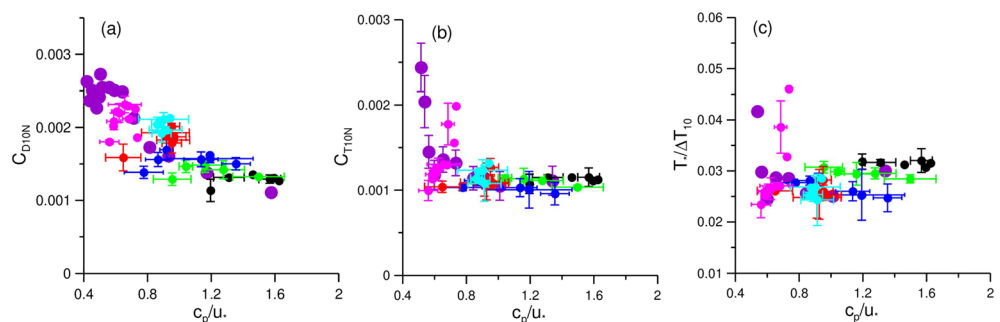


Figure 6. Dependency on the wave age parameter of drag coefficient C_{D10N} (a), heat transfer coefficient C_{T10N} (b), and parameter of the temperature roughness (c). In all panels, the colors follow Figure 4; the violet circles are data of Komori et al. (2018).

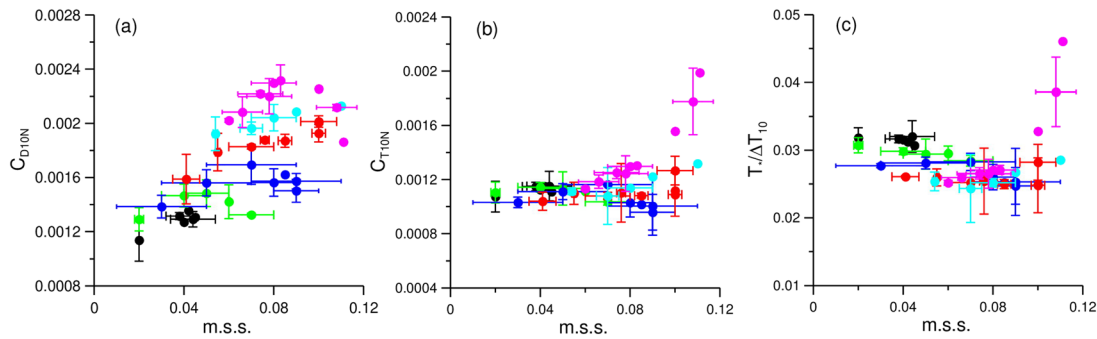


Figure 7. Dependency of the drag coefficient (a), heat transfer coefficient (b), and temperature roughness (c) on m.s.s. In all panels, colors follow Figure 4.

4. The Dependency of Exchange Coefficients on the Parameters of the Waves

To understand what physical factors can cause an increase of the exchange coefficients with increasing air velocity, we analyzed their dependence on the parameters of the wave field. Figures 7a–7c show the dependency of the drag coefficient and logarithm of temperature roughness on m.s.s. One can see a rather significant scatter of the experimental data. In Figures 8a–8c, we plot the dependence of C_{D10N} , C_{T10N} , and the logarithm of the temperature roughness on the dimensionless value $\ln(k_p H_{10})$. When parameterizing the

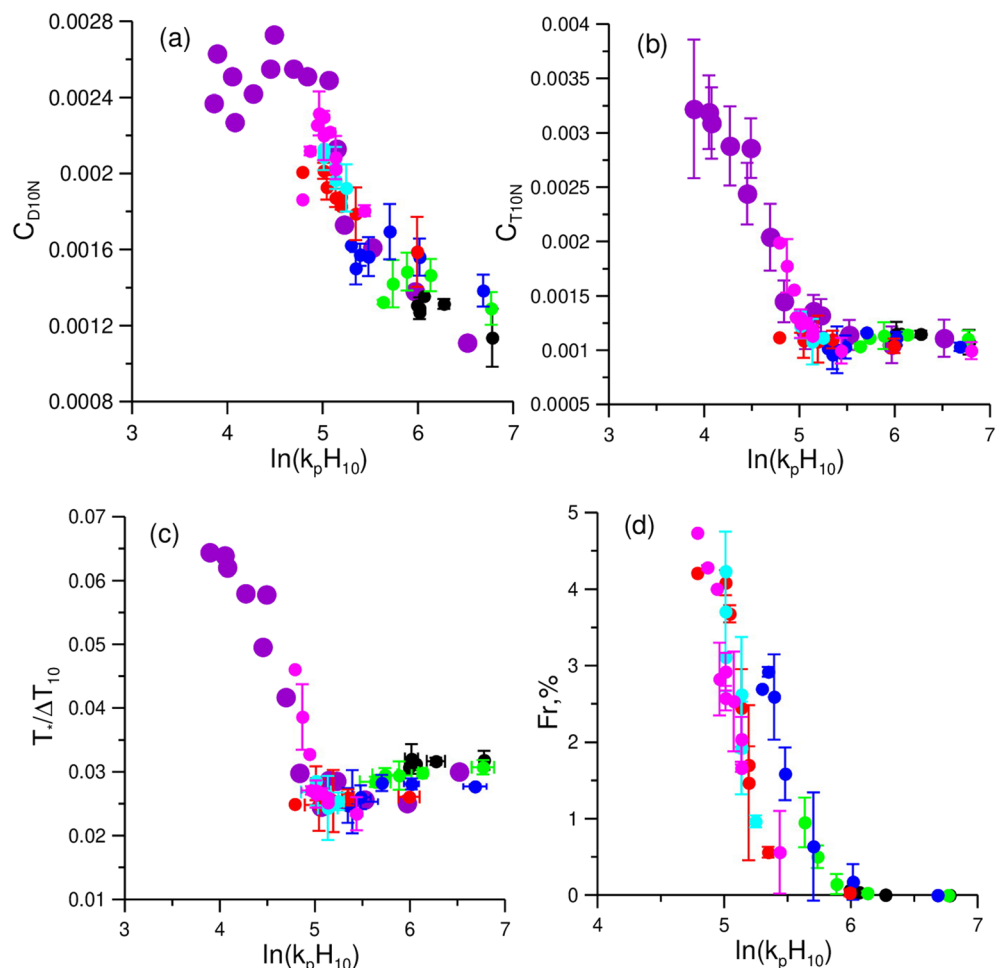


Figure 8. Dependency of the drag coefficient (a), heat transfer coefficient (b), the temperature roughness (c), and the probability of breaking occurrence (d) on dimensionless peak wave numbers. In all panels, colors follow Figure 4.

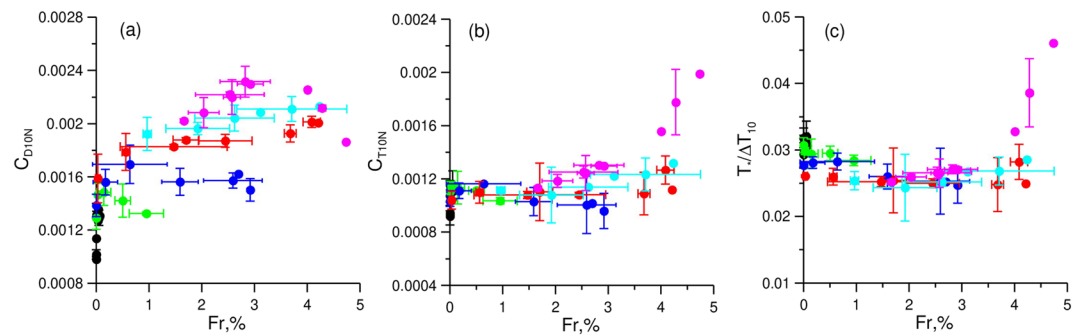


Figure 9. Dependency of the drag coefficient (a), heat transfer coefficient (b), and temperature roughness (c) on the probability of the wave breaking.

exchange coefficients, referred to as the bulk values of the velocity and temperature at 10-m height, this normalization looks natural. In fact, it means that aerodynamic and temperature roughness is a function of wavelength similar to that suggested by Taylor and Yelland (2001). The parameterization by Taylor and Yelland (2001) also depends on the mean slope of the dominant wave $k_p H_s$. Here the later dependence is not manifested, because $k_p H_s$ is constant (see Figure 4b).

A comparison of Figures 7a–7c and Figures 8a–8c shows that representing the data against the peak wave number significantly reduces the spread of the experimental data. It is noteworthy that the data obtained independently at two different facilities (the high-speed wind-wave channel of the IAP RAS and the high-speed basin of the Kyoto University, Komori et al., 2018) using different methods collapse in one curve. One should also consider the fact that in the experiments in the high-speed flume of the Kyoto University, Komori et al. (2018) used unstable stratification of the air flow, while in the present experiments, stratification was stable. Insensitivity of the drag coefficient to the stratification type seems natural since estimates show that the Obukhov scale in all experiments was more than 8 m higher than the height of the airflow above the water surface for both the IAP RAS channel (0.4 m) and in the Kyoto University channel (0.8 m). The similarity of the values of the temperature roughness in the case of stable and unstable stratifications of the atmosphere is an indication of the weak effect of the droplet evaporation on the heat flux, since the phase transition leads to height-dependent cooling of the air, which enhances the stable and attenuates the unstable stratification of the atmosphere.

We also note some peculiarities of the obtained dependency. From Figure 8c, it can be seen that the dominant wind waves are sufficiently short, so that $\ln(k_p H_{10}) > 5$ ($k_p < 0.15 \text{ cm}^{-1}$ or the peak wavelength $\lambda_p < 40 \text{ cm}$) and the Stanton number remains constant. A comparison with Figures 5b and 5c show that, in this case, the temperature roughness is determined by molecular heat transfer at the air-water interface. The assumption by Makin (1998) is satisfied in that the effect of the surface waves on the air-water heat transfer occurs only due to changes in the rates of turbulent transfer and change of the aerodynamic roughness.

It is seen from Figure 8c that at $\ln(k_p H_{10}) < 5$ ($k_p < 0.15 \text{ cm}^{-1}$, the wavelength above 40 cm), the Stanton number and the temperature roughness start increasing sharply with the increase of the wavelengths of the dominant waves and the increase of the significant wave height (Figures 4a and 4b). It indicates a change in the physical properties of the water surface, that leads to increased heat transfer at the air-water interface. To illustrate the nature of these changes, we consider the dependence of the probability of the wave breaking Fr on $\ln(k_p H_{10})$ in Figure 8d. It is seen that at $\ln(k_p H_{10}) < 6$ ($k_p < 0.3 \text{ cm}^{-1}$, the wavelength above 20 cm), there is a sharp increase in Fr , which is defined, according to Longuet-Higgins and Smith (1983), as areas of the water surface with a slope of more than $\theta_{br} = 30.37^\circ$. That is, the change in the physical properties of the water surface, accompanied by an increase in temperature roughness, occurs for longer waves than the beginning of the increase in the probability of wave breaking Fr . This is explained as follows.

It was already noted that the dominant waves have an approximately constant shape with the high steepness equal on average to 0.18 (see Figure 4b). Visual observations show that the shape of such waves is unsteady, the waves are breaking, and the type of wave breaking depends on the wavelength and wind speed. At $F < 35 \text{ s}^{-1}$, the gentle spilling breaker (see Duncan, 2001) dominates when irregular capillary waves arise

Table 2
The Data of the Illustrating Experiment

F, s^{-1}	$u_*, m/s$	$T^*/\Delta T_{10}$	$Fr (\%)$
20	0.48 ± 0.02	0.033 ± 0.001	0
25	0.68 ± 0.03	0.029 ± 0.003	0
30	0.91 ± 0.02	0.025 ± 0.005	0
35	1.34 ± 0.043	0.033 ± 0.015	3.0
40	1.75 ± 0.01	0.062 ± 0.015	8.9
45	2.07 ± 0.03	0.087 ± 0.04	14.9

at the wave crests. Duncan (2001) refers to this regime as the turbulence of capillary waves. At F above $35 s^{-1}$, intense breakings with the entrainment of air bubbles or whitecapping begin to occur. As shown by Troitskaya et al. (2019), the appearance of foam bubbles on the surface of the water causes the increase in the coefficient of resistance of the surface of the water due to the increased aerodynamic drag of surface areas covered with bubbles of foam. This is confirmed by Figure 9a, which plots C_{D10N} versus Fr . When the above-outlined conditions for the presence of whitecapping are met, one can see that C_{D10N} grows with increasing Fr .

Figures 8c and 9c show that with the appearance of whitecapping, the temperature roughness increases, which indicates changes in heat transfer. The effect of whitecapping on the heat exchange was illustrated in a special experiment in which the net was removed. To quantify the strength of whitecapping, the fraction of the water surface covered by foam was measured by the shadow optical method inapplicable in the presence of the net. The technical details of the method and the data processing are described in Troitskaya et al. (2019). The data of the experiment are presented in Table 2. Figure 10a shows substantial growth of the temperature roughness with the increase of the foam coverage. Figure 10b shows that the temperature roughness versus u_* approximately follows Equation 31 for $u_* < 1 m/s$. For $u_* > 1 m/s$, the temperature roughness sharply increases correlating with the strength of whitecapping, which arises at $u_* > 1 m/s$ (see Figure 10c). A similar effect is also demonstrated by Komori et al. (2018), who describe the sharp increase in C_{T10N} while maintaining C_{D10N} (it assumes the increase in temperature roughness) at high wind speeds, implying the presence of whitecapping. The nature of this phenomenon requires further investigation. We speculate that the increase in heat transfer is due to the amplification of the water surface renewal caused by amplification of mixing by whitecapping. Another possible reason for the increase of the heat exchange may be a sharp enhancement of the area of the air-water contact, which occurs during whitecapping. We can also suggest an analogy between the increase in heat transfer and the phenomenon of an anomalous increase in gas exchange at high wind speeds most likely accompanied by whitecapping, which was discussed by Iwano et al. (2013) and Krall and Jähne (2014). This hypothesis requires additional research.

5. Conclusion and Discussion

The most important characteristics that determine the interaction between the atmosphere and ocean are fluxes of momentum, heat, and moisture. For their parameterization, the dimensionless exchange coefficients (the surface drag coefficient C_{D10N} and the heat transfer coefficient or the Stanton number C_{T10N}) are used. Numerous field and laboratory experiments show that C_{D10N} increases with increasing wind speed at moderate and strong wind speeds. As was recently shown (Holthuijsen et al., 2012; Powell et al., 2003), C_{D10N} decreases at hurricane wind speeds. Waves are known to increase the sea surface resistance due to enhanced form drag. The dependence of the heat transfer coefficient C_{T10N} on the wind speed is not certain, and the role of the mechanism associated with the wave disturbances in the mass transfer is not completely

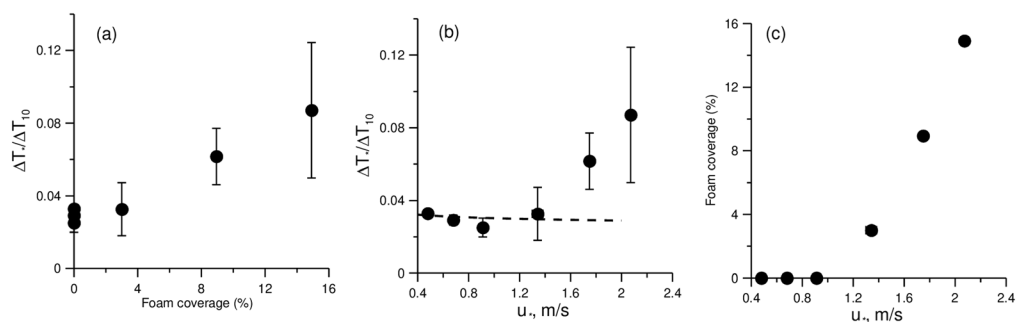


Figure 10. The temperature roughness versus the foam coverage fraction (a) and the wind friction velocity (b) and the foam coverage fraction versus the wind friction velocity (c) obtained in the illustrative experiment without underwater net.

understood. The observations and laboratory data show that this dependence is weaker than for the C_{D10N} and there are differences in the character of the dependence in different data sets. Obviously, the exchange coefficients in field conditions are affected by numerous factors, which cannot be reproduced in laboratory. First of all, the fetch for wind waves in the ocean is dramatically higher than in a laboratory tank. Besides, the amount of sea spray ejected to the atmosphere, which is also fetch dependent, also can be an order of magnitude higher (see, e.g., Troitskaya, Kandaurov, et al., 2018). The advantage of laboratory experiments is in focusing on a certain physical process behind the phenomenon (in our case, the air-water fluxes) under control conditions. This paper focused on the effects of small-scale surface waves on the turbulent exchange of momentum and heat within the laboratory experiment, with the wind and wave parameters maintained and controlled.

The obtained dependency of the surface drag coefficient on the parameters of the experiment was in agreement with previous measurements at high winds by French et al. (2007), Donelan et al. (2004), and Powell et al. (2003). It was mostly described by the wind friction velocity (or the tangential turbulent stress) and increased with both the air flow velocity and wave fetch. The heat exchange coefficient was practically constant at wind speeds below 33–35 m/s in agreement with Jeong et al. (2012) and was accompanied by a decrease of the temperature roughness. It was well described by the dependence on the wind friction velocity, which was obtained by Liu et al. (1979) from the supposition that the heat exchange at the air-water interface is described by the molecular transfer. At wind speeds exceeding 33–35 m/s, both the heat exchange coefficient and temperature roughness sharply increased. These peculiarities are in agreement with recent data from Komori et al. (2018). Moreover, the joint analysis of the data obtained in the high-speed wind-wave channels of the IAP RAS and Kyoto University yields the universal dependency of the exchange coefficients on the peak wave number of surface wave spectra, which assumes the universal dependence of the aerodynamic and temperature roughnesses on the peak wavelength. These dependences are similar to the parameterization of the roughness height suggested by Taylor and Yelland (2001), which includes also the dependence on the mean slope of the dominant wave $k_p H_s$. In the laboratory conditions, the dominant waves are saturated, and $k_p H_s$ is constant. Notably, the effect of the increase of the heat exchange coefficient and temperature roughness did not depend on the type of temperature stratification of the atmospheric boundary layer—which was unstable in the experiments by Komori et al. (2018) and stable in the experiments in the IAP flume.

Joint analysis of the parameters of the surface wave field and the exchange coefficients enables us to conclude that the sharp increase of the heat exchange intensity is associated with increased whitecapping. The physical reasons for this effect are not yet clear. One can suppose the enhancement of the surface renewal due to mixing is associated with whitecapping. Another possible reason may be a sharp increase in the contact area between water and air due to whitecapping. Our study provides a framework for future studies in these critical areas of oceanic and atmospheric research.

Acknowledgments

This work was supported by the Russian Foundation of Basic Research (18-55-50005, 19-05-00249, 18-05-00265, and 18-35-20068) and the Japan Society for the Promotion of Science (JSPS) under the Russia-Japan Research Cooperative Program. Alexander Kandaurov and Olga Ermakova acknowledge partial support from the Russian Science Foundation (agreement no. 19-17-00209). Maxim Vdovin acknowledge support by the President grant for young scientist MK.3184.2019.5. Experiments were performed at the Unique Scientific Facility “Complex of Large-Scale Geophysical Facilities” (<http://www.ckp-rf.ru/usu/77738/>). The authors wish to express their appreciation to professor S. Komori for his valuable comments and advices. The data set for this research is included in this paper (Table 1).

References

- Abramovich, G. N. (1969). *Applied gas dynamics*. Moscow: Nauka Press.
- Ayet, A., Chapron, B., Redelsperger, J. L., Lapeyre, G., & Marié, L. (2020). On the impact of long wind-waves on near-surface turbulence and momentum fluxes. *Boundary-Layer Meteorol.*, 174(3), 465–491. <https://doi.org/10.1007/s10546-019-00492-x>
- Belcher, S. E., Newley, T. M. J., & Hunt, J. C. R. (1993). The drag on an undulating surface induced by the flow of a turbulent boundary layer. *Journal of Fluid Mechanics*, 249, 557–598. <https://doi.org/10.1017/S0022112093001296>
- Brut, A., Butet, A., Durand, P., Caniaux, G., & Planton, S. (2005). Air-sea exchanges in the equatorial area from the EQUALANT99 dataset: Bulk parametrizations of turbulent fluxes corrected for airflow distortion. *Quarterly Journal of the Royal Meteorological Society*, 131(610), 2497–2538. <https://doi.org/10.1256/qj.03.185>
- Coles, D. (1956). The law of the wake in the turbulent boundary layer. *Journal of Fluid Mechanics*, 1(2), 191–226. <https://doi.org/10.1017/S0022112056000135>
- Donelan, M. A., Drennan, W. M., & Magnusson, A. K. (1996). Nonstationary analysis of the directional properties of propagating waves. *Journal of Physical Oceanography*, 26(9), 1901–1914. [https://doi.org/10.1175/1520-0485\(1996\)026<1901:NAOTDP>2.0.CO;2](https://doi.org/10.1175/1520-0485(1996)026<1901:NAOTDP>2.0.CO;2)
- Donelan, M. A., Haus, B. K., Reul, N., Plant, W. J., Stiassne, M., Graber, H. C., et al. (2004). On the limiting aerodynamic roughness in very strong winds. *Journal of Geophysical Research*, 31, L18306. <https://doi.org/10.1029/2004GL019460>
- Drennan, W. M., Zhang, J., French, J. R., McCormick, C., & Black, P. G. (2007). Turbulent fluxes in the hurricane boundary layer. Part II: Latent heat flux. *Journal of the Atmospheric Sciences*, 64(4), 1103–1115. <https://doi.org/10.1175/JAS3889.1>
- Druzhinin, O. A., Troitskaya, Y. I., & Zilitinkevich, S. S. (2015). Stably stratified airflow over a wavy water surface. Part 1: Stationary turbulence regime. *Quarterly Journal of the Royal Meteorological Society*, 142(695), 759–772. <https://doi.org/10.1002/qj.2677>
- Duncan, J. H. (2001). Spilling breakers. *Annual Review of Fluid Mechanics*, 33(1), 519–547. <https://doi.org/10.1146/annurev.fluid.33.1.519>

- Fairall, C. W., Bradley, E. F., Hare, J. E., Grachev, A. A., & Edson, J. B. (2003). Bulk parameterization of air-sea fluxes: Updates and verification for the COARE algorithm. *Journal of Climate*, 16(4), 571–591. [https://doi.org/10.1175/1520-0442\(2003\)016<0571:BPOASF>2.0.CO;2](https://doi.org/10.1175/1520-0442(2003)016<0571:BPOASF>2.0.CO;2)
- French, J. R., Drennan, W. M., Zhang, J. A., & Black, P. G. (2007). Turbulent fluxes in the hurricane boundary layer. Part I: Momentum flux. *Journal of the Atmospheric Sciences*, 64(4), 1089–1102. <https://doi.org/10.1175/JAS3887.1>
- Holthuijsen, L. H., Powell, M. D., & Pietrzak, J. D. (2012). Wind and waves in extreme hurricanes. *Journal of Geophysical Research*, 117, C09003. <https://doi.org/10.1029/2012JC007983>
- Husain, N. T., Hara, T., Buckley, M. P., Yousefi, K., Veron, F., & Sullivan, P. P. (2019). Boundary layer turbulence over surface waves in a strongly forced condition: LES and observation. *Journal of Physical Oceanography*, 49(8), 1997–2015. <https://doi.org/10.1175/JPO-D-19-0070.1>
- Iwano, K., Takagaki, N., Kurose, K., & Komori, S. (2013). Mass transfer velocity across the breaking air-water interface at extremely high wind speeds. *Tellus*, 65(1), 21341. <https://doi.org/10.3402/tellusb.v65i0.21341>
- Janssen, P. A. E. M. (1989). Wave-induced stress and the drag of air flow over sea waves. *Journal of Physical Oceanography*, 19(6), 745–754. [https://doi.org/10.1175/1520-0485\(1989\)019<0745:WISATD>2.0.CO;2](https://doi.org/10.1175/1520-0485(1989)019<0745:WISATD>2.0.CO;2)
- Jeong, D., Haus, B. K., & Donelan, M. A. (2012). Enthalpy transfer across the air-water interface in high winds including spray. *Journal of the Atmospheric Sciences*, 69(9), 2733–2748. <https://doi.org/10.1175/JAS-D-11-0260.1>
- Jones, I., & Toba, Y. (2001). Wind stress over the ocean. In *Wind stress over the ocean*. https://www.researchgate.net/publication/259615822_Wind_Stress_over_the_Ocean
- Komori, S., Iwano, K., Takagaki, N., Onishi, R., Kurose, R., Takahashi, K., & Suzuki, N. (2018). Laboratory measurements of heat transfer and drag coefficients at extremely high wind speeds. *Journal of Physical Oceanography*, 48(4), 959–974. <https://doi.org/10.1175/JPO-D-17-0243.1>
- Krall, K. E., & Jähne, B. (2014). First laboratory study of air-sea gas exchange at hurricane wind speeds. *Ocean Science*, 257–265. <https://doi.org/10.5194/os-10-257-2014>
- Liu, W. T., Katsaros, K. B., & Businger, J. A. (1979). Bulk parameterization of air-sea exchanges of heat and water vapor including the molecular constraints at the interface. *Journal of the Atmospheric Sciences*, 36(9), 1722–1735. [https://doi.org/10.1175/1520-0469\(1979\)036<1722:BPOASE>2.0.CO;2](https://doi.org/10.1175/1520-0469(1979)036<1722:BPOASE>2.0.CO;2)
- Longuet-Higgins, M. S., & Smith, N. D. (1983). Measurement of breaking waves by a surface jump meter. *Journal of Geophysical Research*, 88(C14), 9823–9831. <https://doi.org/10.1029/JC088iC14p09823>
- Lykosov, V. N. (2002). Atmospheric and oceanic boundary layer physics. In I. S. F. Jones, & Y. Toba (Eds.), *Wind stress over the ocean* (pp. 54–81). Cambridge, England: Cambridge University Press.
- Makin, V. K. (1998). Air-sea exchange of heat in the presence of wind waves and spray. *Journal of Geophysical Research*, 103(C1), 1137–1152. <https://doi.org/10.1029/97JC02908>
- Makin, V. K., & Kudryavtsev, V. N. (1999). Coupled sea surface-atmosphere model. Part 1. Wind over waves coupling. *Journal of Geophysical Research*, 104(C4), 7613–7623. <https://doi.org/10.1029/1999JC900006>
- Makin, V. K., Kudryavtsev, V. N., & Mastenbroek, C. (1995). Drag of the sea surface. *Boundary-Layer Meteorology*, 73(1–2), 159–182. <https://doi.org/10.1007/bf00708935>
- Makin, V. K., & Mastenbroek, C. (1996). Impact of waves on air-sea exchange of sensible heat and momentum. *Boundary-Layer Meteorology*, 79(3), 279–300. <https://doi.org/10.1007/bf00119442>
- Monin, A. S., & Yaglom, A. M. (1965). *Statisticheskaya gidromekhanika*, (p. 640). Moscow (in Russian): Nauka.
- Moon, I., Hara, T., Ginis, I., Belcher, S. E., & Tolman, H. L. (2004). Effect of surface waves on air-sea momentum exchange. Part I: Effect of mature and growing seas. *Journal of the Atmospheric Sciences*, 61, 2321–2333. [https://doi.org/10.1175/1520-0469\(2004\)061<2321:EOSWOA>2.0.CO;2](https://doi.org/10.1175/1520-0469(2004)061<2321:EOSWOA>2.0.CO;2)
- Ocampo-Torres, F. J., Donelan, M. A., Merzi, N., & Jia, F. (1994). Laboratory measurements of mass transfer of carbon dioxide and water vapour for smooth and rough flow conditions. *Tellus*, 46(1), 16–32. <https://doi.org/10.1034/j.1600-0889.1994.00002.x>
- Powell, M. D., Vickery, P. J., & Reinhold, T. A. (2003). Reduced drag coefficient for high wind speeds in tropical cyclones. *Nature*, 422(6929), 279–283. <https://doi.org/10.1038/nature01481>
- Takagaki, N., Komori, S., & Suzuki, N. (2016). Estimation of friction velocity from the wind-wave spectrum at extremely high wind speeds. *IOP Conference Series: Earth and Environmental Science*, 35, 012009. <https://doi.org/10.1088/1755-1315/35/1/012009>
- Takagaki, N., Komori, S., Suzuki, N., Iwano, K., Kuramoto, T., Shimada, S., et al. (2012). Strong correlation between the drag coefficient and the shape of the wind sea spectrum over a broad range of wind speeds. *Geophysical Research Letters*, 39, L23604. <https://doi.org/10.1029/2012GL053988>
- Takagaki, N., Komori, S., Suzuki, N., Iwano, K., & Kurose, R. (2016). Mechanism of drag coefficient saturation at strong wind speeds. *Geophysical Research Letters*, 43, 9829–9835. <https://doi.org/10.1002/2016GL070666>
- Taylor, P. K., & Yelland, M. J. (2001). The dependence of sea surface roughness on the height and steepness of the waves. *Journal of Physical Oceanography*, 31(2), 572–590. [https://doi.org/10.1175/1520-0485\(2001\)031<0572:TDOSSR>2.0.CO;2](https://doi.org/10.1175/1520-0485(2001)031<0572:TDOSSR>2.0.CO;2)
- Troitskaya, Y. I., Kandaurov, A., Ermakova, O., Kozlov, D., Sergeev, D., & Zilitinkevich, S. (2017). Bag-breakup fragmentation as the dominant mechanism of sea-spray production in high winds. *Scientific Reports*, 7(1), 1614. <https://doi.org/10.1038/s41598-017-01673-9>
- Troitskaya, Y. I., Druzhinin, O., Kozlov, D., & Zilitinkevich, S. (2018). “Bag-breakup” spume droplet generation mechanism at hurricane wind. Part II. Contribution to momentum and enthalpy transfer. *Journal of Physical Oceanography*, 48(9), 2189–2207. <https://doi.org/10.1175/JPO-D-17-0105.1>
- Troitskaya, Y. I., Ezhova, E. V., & Zilitinkevich, S. S. (2013). Momentum and buoyancy transfer in atmospheric turbulent boundary layer over wavy water surface—Part 1: Harmonic wave. *Nonlinear Processes in Geophysics*, 20(5), 825–839. <https://doi.org/10.5194/npg-20-825-2013>
- Troitskaya, Y. I., Kandaurov, A., Ermakova, O., Kozlov, D., Sergeev, D., & Zilitinkevich, S. (2018). “Bag-breakup” spume droplet generation mechanism at hurricane wind. Part I. Spray generation function. *Journal of Physical Oceanography*, 48(9), 2167–2188. <https://doi.org/10.1175/JPO-D-17-0104.1>
- Troitskaya, Y. I., & Rybushkina, G. V. (2008). Quasi-linear model of interaction of surface waves with strong and hurricane winds. *Izvestiya Atmospheric and Oceanic Physics*, 44(5), 621–645. <https://doi.org/10.1134/S0001433808050083>
- Troitskaya, Y. I., Sergeev, D., Kandaurov, A., Vdovin, M., & Zilitinkevich, S. (2019). The effect of foam on waves and the aerodynamic roughness of the water surface at high winds. *Journal of Physical Oceanography*, 49(4), 959–981. <https://doi.org/10.1175/JPO-D-18-0168.1>

- Troitskaya, Y. I., Sergeev, D. A., Kandaurov, A. A., Baidakov, G. A., Vdovin, M. A., & Kazakov, V. I. (2012). Laboratory and theoretical modeling of air-sea momentum transfer under severe wind conditions. *Journal of Geophysical Research*, 117, C00J21. <https://doi.org/10.1029/2011JC007778>
- Yelland, M., & Taylor, P. K. (1996). Wind stress measurements from the open ocean. *Journal of Physical Oceanography*, 26(4), 541–558. [https://doi.org/10.1175/1520-0485\(1996\)026<0541:WSMFTO>2.0.CO;2](https://doi.org/10.1175/1520-0485(1996)026<0541:WSMFTO>2.0.CO;2)
- Zavadsky, A., & Shemer, L. (2012). Characterization of turbulent airflow over evolving water-waves in a wind-wave tank. *Journal of Geophysical Research*, 117, C00J19. <https://doi.org/10.1029/2011JC007790>
- Zilitinkevich, S. S. (1987). Theoretical model of turbulent penetrative convection. *Izvestiya Atmospheric and Oceanic Physics*, 23(6), 593–610.